Tenth International Conference on Computational Fluid Dynamics (ICCFD10), Barcelona,Spain, July 9-13, 2018

ICCFD10-2018-0310

A higher-order space-time finite-element method for moving-body and fluid-structure interaction problems

L. Diosady*, S. Murman**, C. Carton de Wiart***
Corresponding author: laslo.diosady@nasa.gov

* Science and Technology Corporation, USA.
** NASA Ames Research Center, USA.
*** USRA, USA.

Abstract: We present a high-order finite-element method for moving body and fluid/structure interaction problems. Our solution strategy is based on a space-time discontinuous Galerkin (DG) spectral-element discretization which extends to arbitrary order of accuracy. The space-time DG discretization is a natural choice for moving body and fluid-structure interaction problems as moving surfaces are incorporated simply by considering curved space-time elements whose space-time faces align with the moving body. We present a discontinuous-Galerkin in time discretization for six-degree of motion modeling of rigid bodies, and a continuous-Galerkin discretization for equations of linear elasticity to generate curved space-time meshes. Numerical results for several simple 2D test cases are presented in order to verify the implementation of the different models. Finally we present a preliminary dynamic simulation of a parachute.

Keywords: Numerical Algorithms, Computational Fluid Dynamics, High-order.

1 Introduction

Accurate modeling of fluid-structure interactions is important in many aerospace systems (i.e. parachute-dynamics, flutter analysis, etc). Higher-order numerical methods can provide greater efficiency for these simulations requiring high spatial and temporal resolution, allowing for solutions with fewer degrees of freedom and lower computational cost than traditional second-order methods. In our recent work, we have been developing a high-order space-time discontinuous-Galerkin finite-element method for high-Reynolds-number compressible turbulent flow simulations [1, 2, 3, 4, 5]. We have recently enhanced our solver's capability to solve higher-order continuous- and C1-discontinuous- Galerkin discretizations for solid-mechanics problems [6, 7], and developed a framework for the monolithic solution of coupled multi-physics problems [8]. We have shown the advantage of using higher-order methods for compressible turbulent flows [1, 2, 4] and our desire is to take advantage of higher-order methods for the simulation of coupled fluid/structures interaction problems. In this work we present preliminary work using our monolithic space-time finite-element framework to solve moving-body and fluid/structure interaction problems.

In a space-time formulation the entire 4-dimensional (3-spatial + time) space-time domain is discretized using finite elements with polynomials in both space and time [9, 10, 11, 12, 13, 14, 15]. For fixed domain simulations, the spatial mesh is simply extruded in the temporal direction to form the space-time mesh. However, a space-time finite element formulation can be naturally extended for moving domain problems by deforming the spatial boundaries of the space-time mesh as a function of time. By treating the spatial and temporal discretization in a unified manner, the resulting discretization guarantees the satisfaction of the geometric conservation law (provided sufficient integration is used) [16]. This has made the space-time formulations a natural choice for moving domain and FSI simulations [9, 10, 14, 15].

The reduced numerical stabilization present in higher-order schemes implies that special care needs to be taken in the development of numerical methods to suppress nonlinear instabilities. Inconsistent coupling

of fluid and structure can lead to numerical instabilities and catastrophic failure of the simulation [17, 9, 12]. Typically, numerical methods for FSI problems are based on partitioned schemes; separate solvers are developed for each discipline, leveraging expertise and existing software for each domain. Coupling of multiple disciplines is often performed as an after-thought, with coupling schemes which may be non-conservative, inaccurate or numerically unstable [18]. Monolithic approaches solve the complete system of equations corresponding to the coupled FSI problem simulatenously [11, 18]. As such, monolithic approaches may be designed to be conservative, higher-order and stable[11, 12].

Our numerical scheme for the fluid is based on a nonlinearly-stable space-time discontinuous-Galerkin method which has been used to perform turbulent flow simulations up to 16th-order accuracy in space and time [4]. In order to ensure conservative coupling between fluid and structural domains we have been developing structural models discretized with finite-element methods which are conjugate to our fluid solver. In particular, we have developed a linear-elastic analogy solved using a higher-order continuous finite-element discretization to generate iso-parametric space-time elements [6]. The structure may be modeled using this same linear-elastic discretization, or alternatively for thin shells we have developed a C^1 discontinuous linear-shell model [7]. In this work we also develop a six degree-of-freedom (6-DOF) solver for rigid body displacement, also based on a discontiuous-Galerkin formulation. By choosing a structural model based on a space-time finite-element space which is conjugate to our fluid solver we can ensure discrete conservation of energy in the coupled FSI problem. Finally, we use a monolithic solution approach, which can ensure non-linear stability of the fully coupled problem [9, 12].

In this paper we present preliminary verification of our space-time discontinuous Galerkin solver for moving body simulations. In Section 2 we present the discretization for the fluid domain, the 6-DOF solver and the linear elasticity approach for generating curved space-time domains. In Section 3 we discuss our monolithic solution strategy. In Section 4 we present numerical results for several simple verification studies as well as a preliminary dynamic simulation of a parachute. Finally we present conclusions and future outlook in Section 5.

2 Discretization

2.1 Fluid Domain

For the fluid domain we solve the compressible Navier-Stokes equations written in conservative form as

$$\boldsymbol{u}_{,t} + \left(\boldsymbol{F}^{Inv} - \boldsymbol{F}^{Visc}\right)_{,i} = 0, \tag{1}$$

where $\boldsymbol{u} = [\rho, \rho u_j, \rho E]$ is the conservative state vector, with ρ the density of the fluid, u_j the velocity components and E the total energy. The inviscid and viscous fluxes are given respectively by

$$\boldsymbol{F}^{Inv} = \begin{bmatrix} \rho u_i \\ \rho u_j u_i + p\delta_{ij} \\ \rho H u_i \end{bmatrix} \qquad \boldsymbol{F}^{Visc} = \begin{bmatrix} 0 \\ \tau_{ij} \\ \tau_{ij} u_j + \kappa_T T_{,j} \end{bmatrix} \tag{2}$$

where p is the static pressure, δ_{ij} the Kronecker delta, H the total enthalpy, τ_{ij} the viscous stress tensor, T the temperature and κ_T the thermal conductivity. The system is closed using the following relationships

$$T = \frac{p}{\rho R}, \qquad p = (\gamma - 1)\left(\rho E - \frac{1}{2}\rho u_k u_k\right), \qquad \tau_{ij} = \mu(u_{i,j} + u_{j,i}) - \lambda u_{k,x_k}\delta_{ij}, \tag{3}$$

where R is the gas constant, γ the specific heat ratio, μ the dynamic viscosity and $\lambda = \frac{2}{3}\mu$ the bulk viscosity.

We use a space-time discontinuous-Galerkin discretization of (1). The domain Ω is partitioned into elements κ, while time is partitioned into time-intervals (time-slabs) I. We seek a solution $\boldsymbol{u}$ which satisfies the weak form

$$\sum_{\kappa}\left\{\int_I\int_\kappa -\left(\boldsymbol{w}_{,t}\boldsymbol{u} + \boldsymbol{w}_{,i}(\boldsymbol{f}_i^I - \boldsymbol{f}_i^V)\right) + \int_I\int_{\partial\kappa}\boldsymbol{w}(\widehat{\boldsymbol{f}_i^I\boldsymbol{n}_i} - \widehat{\boldsymbol{f}_i^V\boldsymbol{n}_i}) + \int_\kappa \boldsymbol{w}(t_-^{n+1})\boldsymbol{u}(t_-^{n+1}) - \boldsymbol{w}(t_+^n)\boldsymbol{u}(t_-^n)\right\} = 0 \tag{4}$$

where the second and third integrals arise due to the spatial and temporal discontinuity, respectively, of the basis functions. $\widehat{\boldsymbol{f}_i^I \boldsymbol{n}_i}$ and $\widehat{\boldsymbol{f}_i^V \boldsymbol{n}_i}$ denote single valued numerical flux functions approximating, respectively, the inviscid and viscous fluxes at the spatial boundaries of the elements. For fixed domains problems, the elements κ are fixed in time, and the space-time elements corresponding to $I \times \kappa$ have "temporal faces" which are orthogonal to the spatial direction and "spatial faces" which are orthogonal to the temporal direction. For moving body simulations, we use a slab-based approach where the temporal faces remain orthogonal to the spatial direction, however the spatial faces vary in time (i.e. are not orthogonal to the temporal direction). Hence the space-time faces over which we integrate in the second term in (4) have normals with components in the temporal direction and a fully 4-dimensional space-time flux must be computed. In this work we compute the space-time flux by upwinding the temporal component, while computing the spatial component using the inviscid flux of Ismail and Roe [19] and a viscous flux using an interior penalty method, where the penalty parameter is computed in a manner that is consistent with the second method of Bassi and Rebay [20].

In order to ensure stability we use an entropy variable formulation where we seek solutions which are polynomial approximations of the entropy variables, $\mathbf{v} \in \mathcal{V}^p$, such that the conservative variables are given through the mapping $\boldsymbol{u}(\mathbf{v}_h)$. The space $\mathcal{V}^p$ is spanned by the tensor-product of 1D Lagrange basis functions defined at the Gauss-Legendre points. Under exact integration, this space-time DG discretization satisfies a discrete Clausius-Duhem inequality ensuring discrete satisfaction of the second law of thermodynamics [21]. In particular, this allows for the proof of a nonlinear entropy-stability for the numerical scheme [21]. In practice, integrals appearing in (4) are approximated with numerical quadrature rules using twice as many points as solution coefficients in each dimension, which has been sufficient in our previous work [4].

2.2 6-DOF Discretization

We initially consider the motion of a rigid body acting under the influence of forces exerted by the fluid. The motion of a rigid body, commonly referred to as six-degree of freedom (6-DOF) motion, is computed by solving Newton's equations for the translation of the center of gravity and Euler's equations for the rotation about a centroidal axis (see for example [22]). Specifically, for the translation we solve for the position, $\mathbf{x}_{cg}$, and velocity, $\mathbf{v}_{cg}$, of the center of gravity using:

$$\begin{aligned} \mathbf{x}_{cg,t} &= \mathbf{v}_{cg} \\ \mathbf{v}_{cg,t} &= \boldsymbol{f}/m \end{aligned} \tag{5}$$

where $\boldsymbol{f}$ is the applied force while m is the mass. The orientation of the body can be expressed using displacement ϕ about an axis of rotation $\boldsymbol{a}$. The orientation is most conveniently expressed using the Euler parameters $\mathbf{e} = \begin{bmatrix} e_0 & e_1 & e_2 & e_2 \end{bmatrix}^T$, where

$$e_0 = \cos\tfrac{\phi}{2} \tag{6}$$

$$e_1 = a_x \sin\tfrac{\phi}{2} \tag{7}$$

$$e_2 = a_y \sin\tfrac{\phi}{2} \tag{8}$$

$$e_2 = a_z \sin\tfrac{\phi}{2} \tag{9}$$

The rotation of the body is obtained by solving the following equations for the Euler parameters and angular velocity ω:

$$\begin{aligned} I\omega_{,t} + \omega \times (I\omega) &= \mathbf{M} \\ \mathbf{e}_{,t} &= \tfrac{1}{2}\boldsymbol{L}^T\omega \end{aligned} \tag{10}$$

where I is the moment of inertia, $\mathbf{M}$ is the externally applied moment, while $\boldsymbol{L}^T$ is given in terms of the Euler parameters as:

$$\boldsymbol{L}^T = \begin{bmatrix} -e_1 & -e_2 & -e_3 \\ e_0 & -e_3 & e_2 \\ e_3 & e_0 & -e_1 \\ -e_2 & e_1 & e_0 \end{bmatrix} \tag{11}$$

Equations (5) and (10) correspond to a system of coupled first-order ordinary differential equations which are forced by the fluid through the terms $\boldsymbol{f}$ and $\mathbf{M}$. In turn, the displacement (and velocity) of the rigid body couples back to the fluid problem through the definition of the space-time mesh. While many possible choices are available to integrate these equations of motion, we implement a discontinuous-Galerkin in time discretization so that our discretization of the 6-DOF motion is conjugate with that used for our fluid solver. Namely, the polynomial representation of the forces, displacements and velocities are consistent between the fluid and 6-DOF solver. We use the 6-DOF motion to define the space-time mesh for the fluid domain. In particular, the space-time mesh is obtained from an initial mesh by applying an affine transformation to the polynomial representation of the coordinates of the initial mesh. Using a nodal basis in the temporal direction, the transformation is applied independently for each temporal nodal location. The procedure results in a fully curved isoparametric space-time mesh appropriate for the space-time fluid solver.

2.3 Elasticity

When considering more complicated fluid-structure interaction involving structural deformation, we wish to directly generate a curved isoparametric space-time mesh. We solve the equations of linear elasiticity to obtain the volume displacement of the fluid mesh given the prescribed motion of the surface (or part of the surface) of the fluid mesh. The equations of linear elasticity are

$$\sigma_{ij,j} = 0 \tag{12}$$

where σ_{ij} is the Cauchy stress tensor given by

$$\sigma_{ij} = 2\mu_e \epsilon_{ij} + \lambda_e \epsilon_{kk} \tag{13}$$

$\mu_e = \frac{E}{2(1+\nu)}$ and $\lambda_e = \mu_e \frac{2\nu}{1-2\nu}$ are the Lamé constants given as a function of the Young's Modulus, E, and Poisson ratio, ν. The strain tensor, ϵ is given by

$$\epsilon_{ij} = \tfrac{1}{2}\left(u_{i,j} + u_{j,i}\right) \tag{14}$$

where $\boldsymbol{u}$ is the displacement field. A compact representation of the stress tensor may be given by $\sigma_{ij} = \mathbf{C}^{ijkl} u_{i,j}$, where $\mathbf{C}^{ijkl}$ is the stiffness tensor. We note that we could include an acceleration term in (12) and solve the equations of linear elasticity as a structural model, though we have yet to apply it for this purpose. When applying the linear elasticity model for mesh deformation the parameters E and ν may be varied spatially to improve mesh quality. A common choice, employed here, is to fix ν and vary E on each element proportionally with the inverse of the Jacobian of mapping from reference to physical space [13].

We apply a continuous finite element discretization of (12) over the initial mesh of the fluid domain. Define $\mathcal{V} = \left\{\boldsymbol{w} \in \mathcal{H}_1(\Omega \times I), \boldsymbol{w}|_\kappa \in [\mathcal{P}(\kappa \times I)]^3\right\}$, the space-time finite-element space consisting of $\mathcal{C}^0$ continuous piece-wise polynomial functions on each element.

We seek solutions $\boldsymbol{u} \in \mathcal{V}_E$ satisfying

$$\sum_\kappa \left\{ -\int I \int_{\kappa^0} \boldsymbol{w}_{i,j} \mathbf{C}^{ijkl} \boldsymbol{u}_{k,l} + \int_I \int_{\partial\kappa^0 \cap \partial\Omega} \boldsymbol{w}_i \widehat{\mathbf{C}^{ijkl} \boldsymbol{u}_{k,l}} \boldsymbol{n}_j \right\} = 0. \tag{15}$$

We note that the integration is performed over the initial spatial mesh (i.e elements κ^0) of the fluid domain extruded in time, as opposed to the deformed mesh. An alternative approach is to integrate over the initial spatial mesh for each time-slab, which may potentially allow for larger mesh deformations. However, this

later approach results in a scheme where the mesh deformation is a function of not only the given boundary displacement but the entire displacement history.

3 Solution Strategy

We have chosen to discretize the fluid, 6-DOF and linear-elasticity equations using space-time finite-element methods which are conjugate to one another. In order to ensure discrete conservation of energy we use a monolithic solver for the coupled fluid-structure problem. Consider for example the coupled fluid/6-DOF solver. We denote by U_{NS} and U_{6DOF} the discrete unknowns associated with the fluid and 6-DOF solver respectively. The corresponding residual statements for the fluid and 6-DOF solver can be written accordingly as:

$$R_{NS}(U_{NS}, \alpha_{6DOF-NS}) = 0 \quad (16)$$

$$R_{6DOF}(U_{6DOF}, \alpha_{NS-6DOF}) = 0 \quad (17)$$

where $\alpha_{6DOF-NS}$ and $\alpha_{NS-6DOF}$ denote the data required for coupling the two different models. We denote by U the vector of all unknowns (fluid/6-DOF/etc.) and solve the coupled problem:

$$R(U) = 0 \quad (18)$$

We solve (18) using a Jacobian-free Newton-Krylov approach, where at each Newton iteration we obtain an update of the solution by solving a linear system using GMRES. Each step of GMRES requires the application of the Jacobian matrix to a vector which is equivalent to a linearized residual evaluation. We note that the exact linearized residual involves propagating the sensitivity with respect to both U and α through the residual statement for the discretization of each physics module. Thus the different models are coupled both through the nonlinear and linear residual evaluation. Details of the coupling procedure is given in [8].

4 Numerical Results

In this section we present initial numerical results for some verification tests performed using our finite-element framework.

4.1 Heaving/Pitching Airfoil

In the first set of numerical test cases we validate the space-time DG formulation for solving moving body problems with prescribed motion. We consider the heaving/pitching airfoil problem from the International Workshop on higher-order CFD methods [23, 24] (case CL1). The three test cases involve flow over a NACA0012 airfoil at $M = 0.2$, $Re = 1000$, starting initially from a steady-state solution with prescribed motion corresponding to: 1. pure heaving, 2. flow aligning and 3. energy extracting motions. The equations for the displacement and rotation about 1/3 chord are given in terms of non-dimensional time units are presented in Table 1. Figure 1 show the images of the solution at several time instances throughtout the motion.

Case 1 (Heaving)	Case 2 (Flow Aligning)	Case 3 (Energy Extracting)
$h_1(t) = t^2(3-t)/4$	$h_2(t) = t^2(3-t)/4$	$h_3(t) = t^3(-8t^3 + 51t^2 - 111t + 84)/16$
$\theta_1(t) = 0^\circ$	$\theta_2(t) = t^2(t^2 - 4t + 4)60^\circ$	$\theta_3(t) = t^2(t^2 - 4t + 4)80^\circ$

Table 1: Heaving/Pitching airfoil case parameters

We validate our space-time DG scheme by computing two integral outputs: 1. the work which the fluid exerts on the airfoil and 2. the vertical impulse from the fluid onto the airfoil. These are given respectively

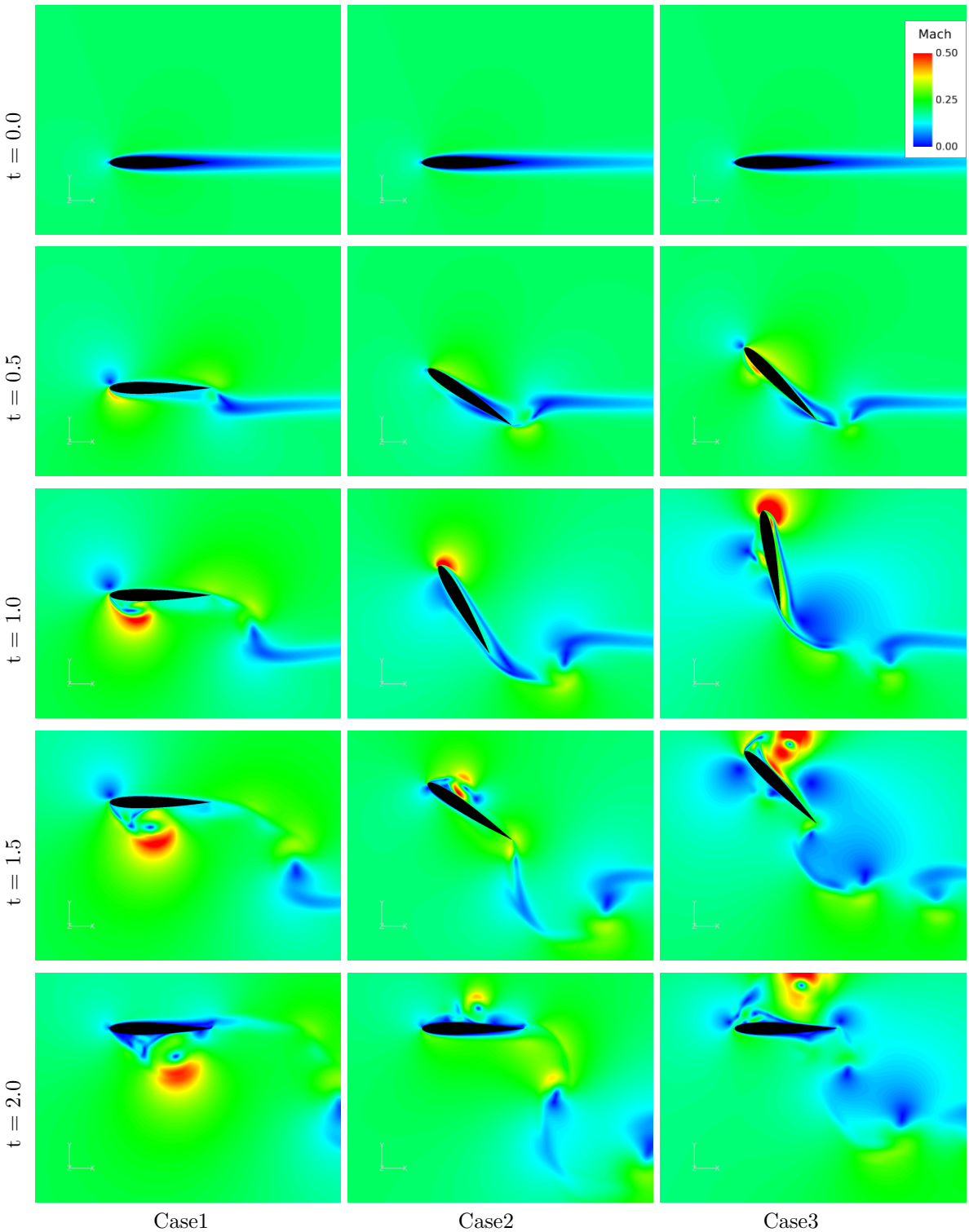


Figure 1: Mach number contours from heaving/pitching airfoil test cases.

by:

$$W = \int_0^T \int_{\text{airfoil}} \vec{v}(t) \cdot \vec{f}(t) ds dt \tag{19}$$

$$I = \int_0^T \int_{\text{airfoil}} f_y ds dt \tag{20}$$

where $\vec{v}$ is the velocity of the surface while $\vec{f} = [f_x, f_y]$ is the force imparted by the fluid on the airfoil. In Table 2 we report the values of work and impulse computed using our space-time DG scheme on the finest mesh considered as well as corresponding results from the 5th International Workshop on higher-order CFD methods [24]. The present results fall within the range of the reported values and show particularly good agreement with the results from UC Berkeley.

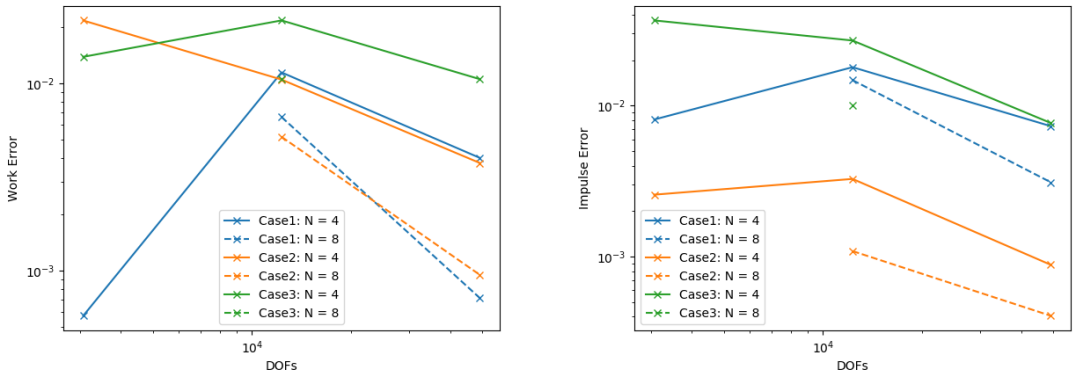
Group	UC Berkeley	U. Michigan	Onera	NASA (Current)
Case1, Work	-1.409	-1.384	-1.405	-1.412
Case1, Impulse	-2.376	-2.331	-2.373	-2.380
Case2, Work	-0.220	-0.205	-0.209	-0.221
Case2, Impulse	0.590	0.610	0.591	0.593
Case3, Work	0.401	0.364	0.334	0.396
Case3, Impulse	1.695	1.670	1.708	1.693

Table 2: Computed output quantities from 5th International Workshop on higher-order CFD and current results [24]

The source of the small discrepencies between the results computed by different groups at the higher-order workshop has yet to be satisfactorily determined. As a result, each participant at the higher-order workshop presented convergence results relative to a truth value computed using a highly refined mesh using their numerical scheme [24]. We report convergence results in the same manner. Figure 2 shows the convergence of the work and impulse outputs using our DG scheme with 4th and 8th order space-time elements. Due to the lack of solution regularity for this test case we do not expect to achieve formal order of accuracy for our higher order schemes. However, we observe that the 8th order scheme generally has lower error in the work output than the 4th order scheme for a given number of degrees of freedom (the exception is case 1 at 4th order where the fortuitous cancellation of forces causes the coarsest grid to appear to have the smallest work error). Additionally, the convergence rate of the 8th order scheme appears to be better than the 4th order scheme . Similarly, for the impulse output, the 8th order scheme has lower absolute error versus the 4th order scheme for a given number of degrees of freedom, however, the trend in the convergence rate is less clear.

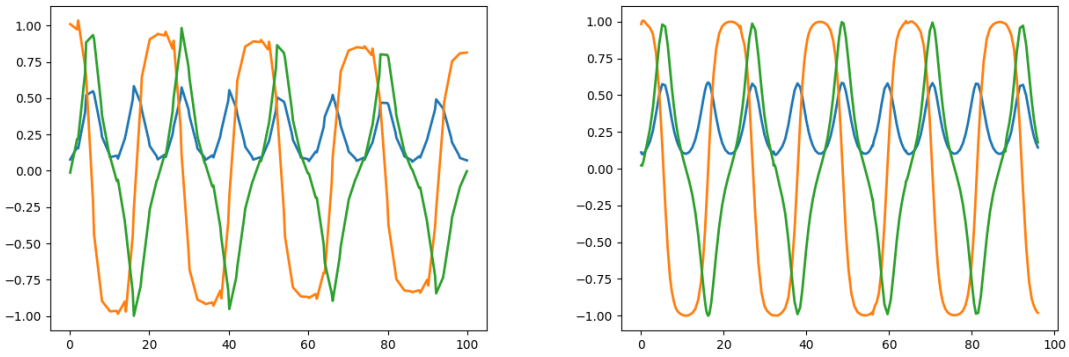
4.2 6-DOF verification

We next consider verification of the space-time implementation of 6-DOF solver. We consider two verification test cases from Murman et al. [22]. First, we consider translational motion corresponding to applying a constant external force. The exact solution corresponds to a displacement which is a quadratic function of time. Thus, our space-time DG scheme should reproduce the exact solution when using quadratic or higher order polynomials. We have verified that this is indeed the case. Next, we consider a test case corresponding to the spining motion of a block in the absence of external forces. Rotation about the semi-major axis is unstable resulting in a tumbling motion for which an analytic solution is available. Figure 3 plots the angular velocity for the tumbling motion solved using 2nd and 8th order schemes with a fixed number of degrees of freedom. As can be seen the large numerical dissipation of the 2nd order scheme results in damping of the angular momentum, while 8th order scheme is much less dissipative. Figure 4 shows the corresponding error convergence using 2nd, 4th and 8th order schemes. The numerical experiment shows the we recover the formal order of accuracy of the scheme.



(a) Work convergence (b) Impulse convergence

Figure 2: Error convergence plots for heaving/pitching airfoil test cases.



(a) $N = 2$ (b) $N = 8$

Figure 3: Angular velocity for 6DOF verification of tumbling motion about semi-major axis

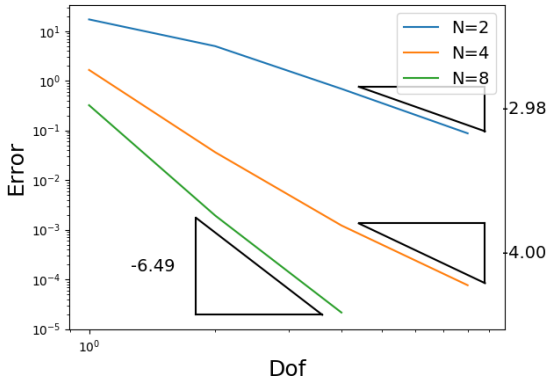


Figure 4: Error convergence for 6-DOF verification of tumbling motion about semi-major axis

4.3 Coupled Fluid/6-DOF

Next we verify the coupled fluid/6-DOF model. In the absence of verification cases with analytical solutions, we consider the motion of a NACA0012 airfoil under the influence of gravity. We consider several test cases corresponding to different values for the center of gravity, mass and moment of inertia. In the first set of test cases we verify the asymptotic behaviour of the coupled fluid/6-DOF problem under a constant gravitational force. We first compute the drag on the NACA0012 airfoil at zero angle of attack, $M = 0.2$ and $Re = 1000$. We then solve a coupled fluid/6-DOF problem where we set the center of gravity to be a point on the leading edge of the airfoil and choose the mass such that the gravitational force will be equivalent to the computed drag. Thus, the coupled fluid/6-DOF problem should result in a terminal velocity matching the steady-state problem. We consider three test cases: 1. the airfoil is initially aligned with the gravitational force and 2. the airfoil is orthogonal to the gravitational force with a small moment of inertia and 3. with large moment of inertia. Figure 5 shows selected images from the simulation, while Figure 6 plots the corresponding velocity, and angle for the three cases. While the initial motion is significantly different for the three test cases, the expected asymptotic behaviour is reached in each case.

Next we consider moving the location of the center of gravity along the airfoil. Again we consider three test cases, with the center of gravity located at: 1. the leading edge, 2. slightly fore of the aerodynamic center and 3. slighlty aft of the aerodynamic center. Figure 7 plots the trajectories of the airfoil for these test cases and the corresponding velocity and orientation. With the center of gravity located at the leading edge, we recover the terminal velocity test case above. With the center of gravity located slightly fore of the aerodynamic center we recover an asymptotic trajectory with a constant glide slope. Finally, with the center of gravity aft of the aerodynamic center we recover an unstable feather-like trajectory. Figure 8 shows images from this trajectory.

4.4 Heaving/Pitching Airfoil using Elasticity Mesh Deformation

Next we solve the heaving/pitching airfoil test case using linear elasticity to deform the mesh. The displacement of the surface of the airfoil is specified, while the location of the space-time mesh is determined using the linear-elasticity solver. We solve test case 2 from the higher-order workshop using a 4th order space-time mesh. Figure 9 depicts the initial 4th order mesh, along with the space-time mesh deformed using elasticity at several temporal locations throughout the heaving/pitching motion. Displacing the interior nodes of the mesh the linear elastic model, with Poisson ratio of $\nu = 0.4$ and Young's modulus scaled with the inverse of the Jacobian determinant, ensures valid elements everywhere in the domain despite the large deformations due to the prescribed motion. We quantify the quality of the mesh by plotting the determinant of the deformation gradient tensor near the surface of the airfoil. As can be seen, the linear-elastic model maintains high quality elements throughout the domain with the deformation tensor near unity everywhere in the domain except for some significant deformation near the trailing edge. Using a Young's modulus scaled inversely with the Jacobian determinant ensures near rigid body motion near the airfoil surface as we generally have small elements here, while larger deformations are allowed further from the airfoil surface where there are larger elements.

4.5 Dynamic Parachute Simulation

Finally, use our space-time discontinuous Galerkin scheme to performs a dynamic parachute simulation. In this preliminary result we consider only rigid body displacement with a predefined motion. For this preliminary simulation we consider a 2nd order spatial and 4th order temporal discretization for the fluid. The prescribed mesh motion corresponds to a pendulum-like motion as seen in recent parachute drop tests [25]. Figure 10 shows images from the dynamic simulations. Ultimately, the goal of this work is to model the full dynamics of the parachute motion, while this work represents one step in this direction.

5 Conclusion and Future Work

We presented a higher-order space-time finite element discontinuous-Galerkin method for performing moving body and fluid-structure interaction simulations. The space-time DG formulation extends naturally to

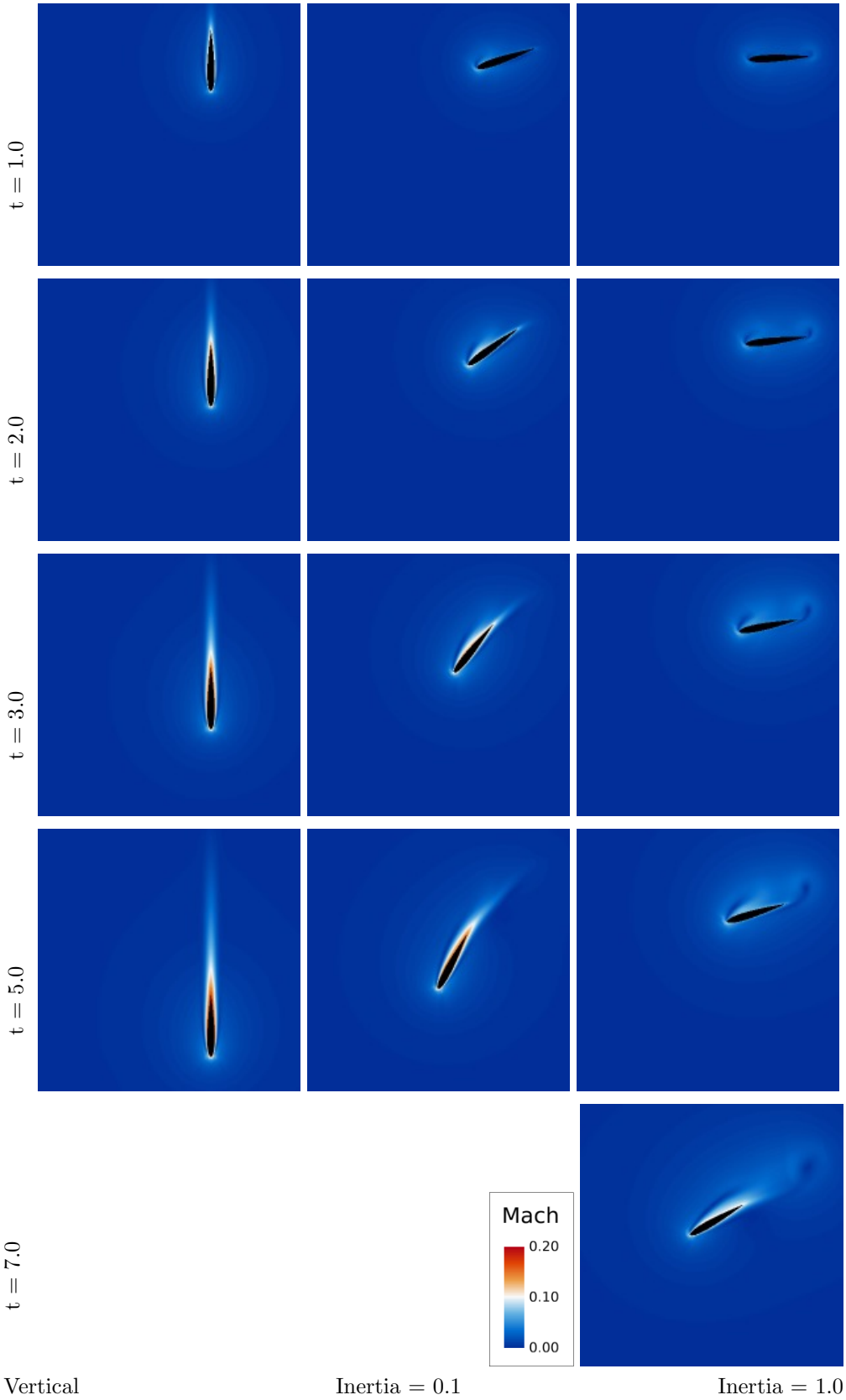
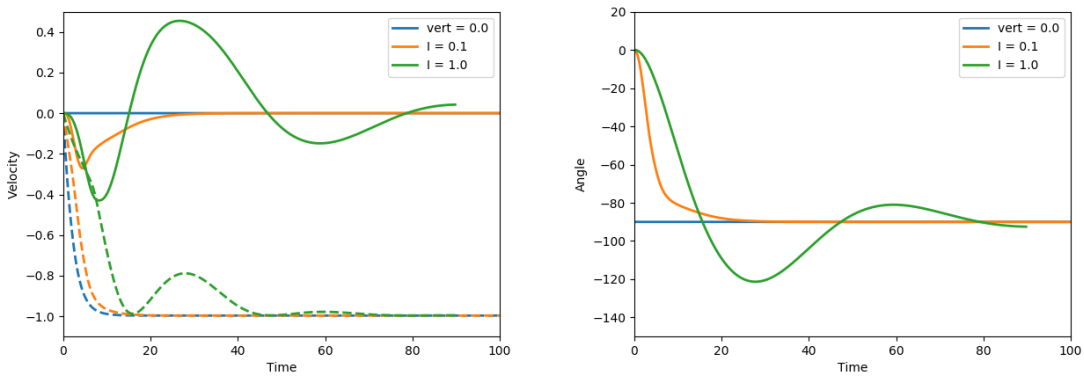
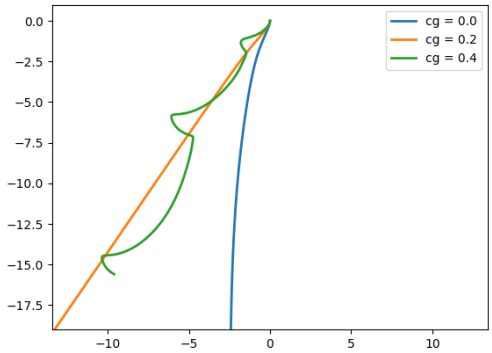


Figure 5: Images from terminal velocity fluid/6dof verification

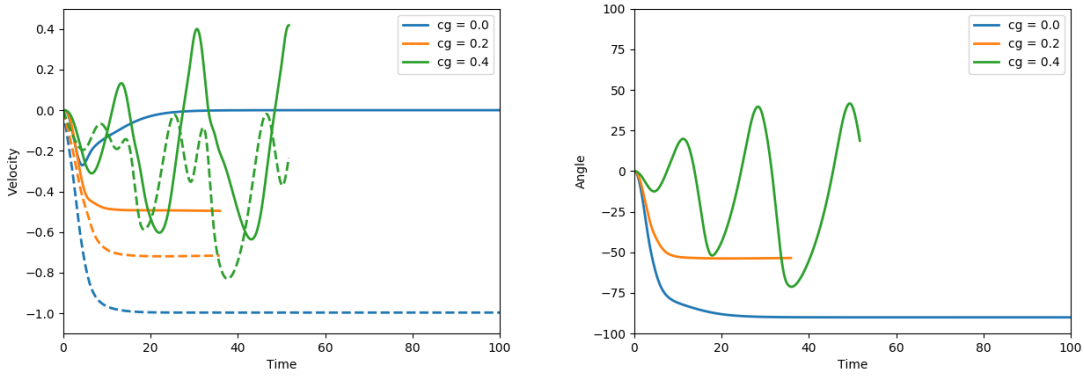


(a) Velocity (b) Angle

Figure 6: Velocity and orientation for terminal velocity fluid/6-DOF verification

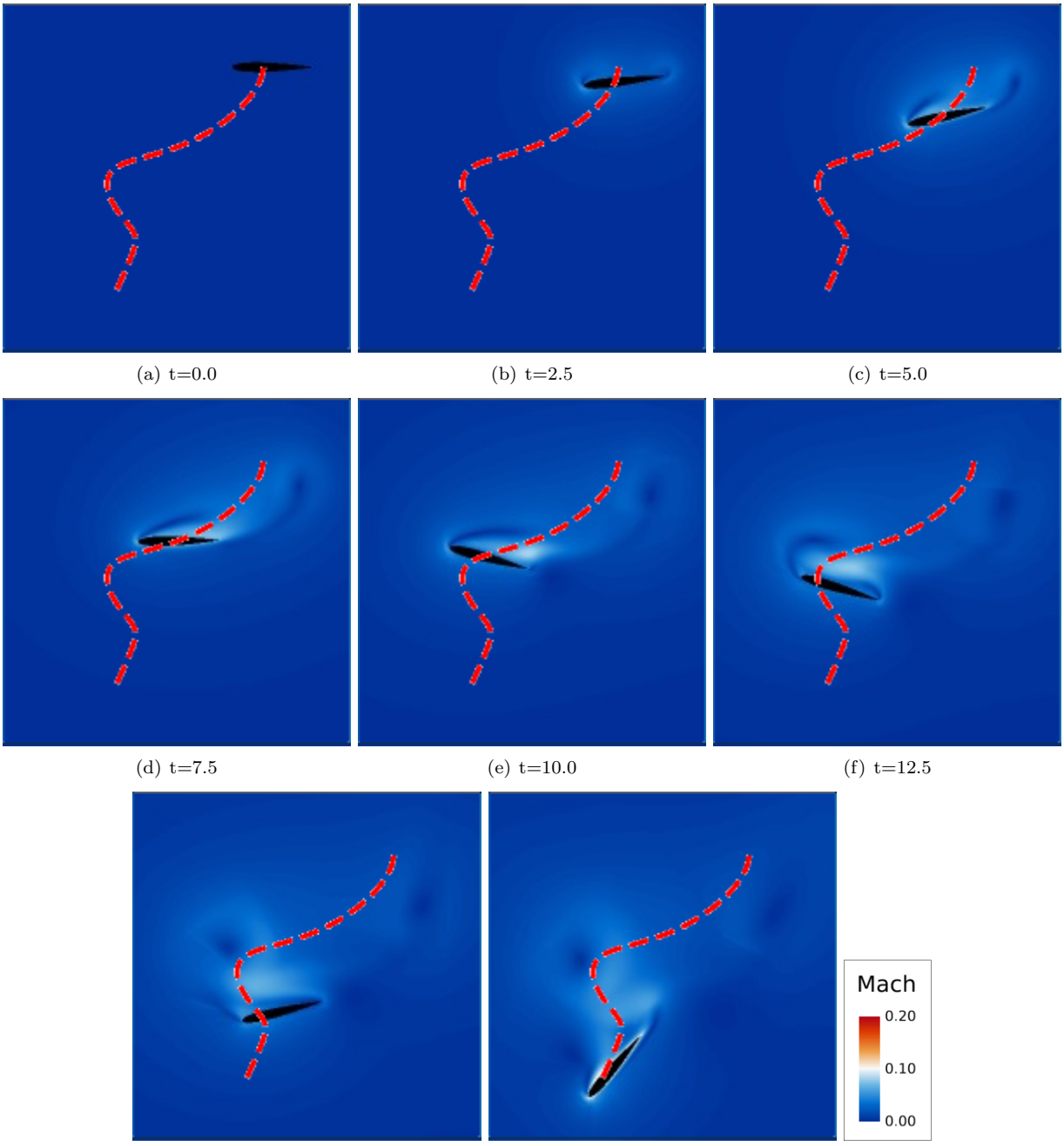


(a) Trajectory



(b) Velocity (c) Angle

Figure 7: Velocity and orientation for fluid/6-DOF verification with different center of gravity locations

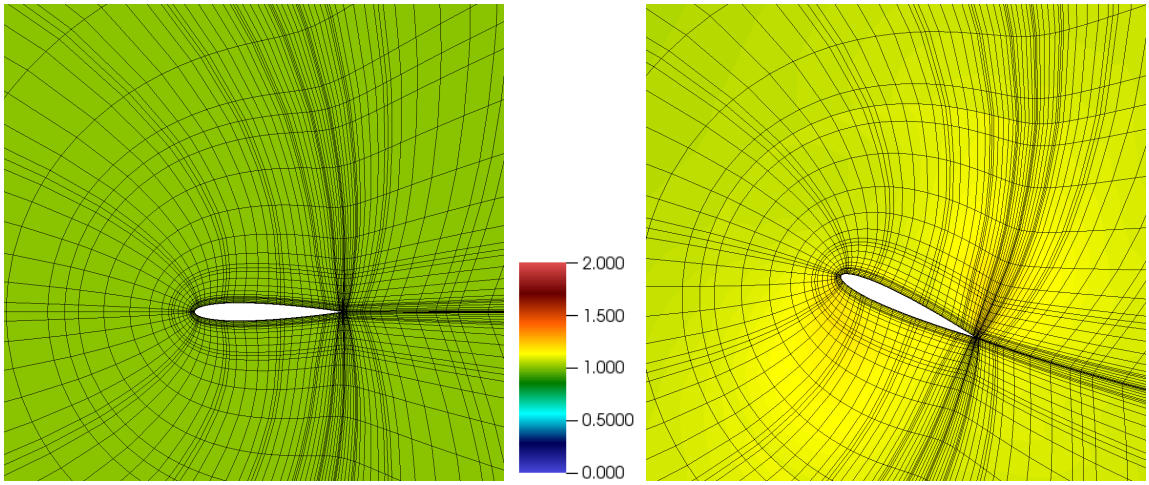


(a) t=0.0 (b) t=2.5 (c) t=5.0

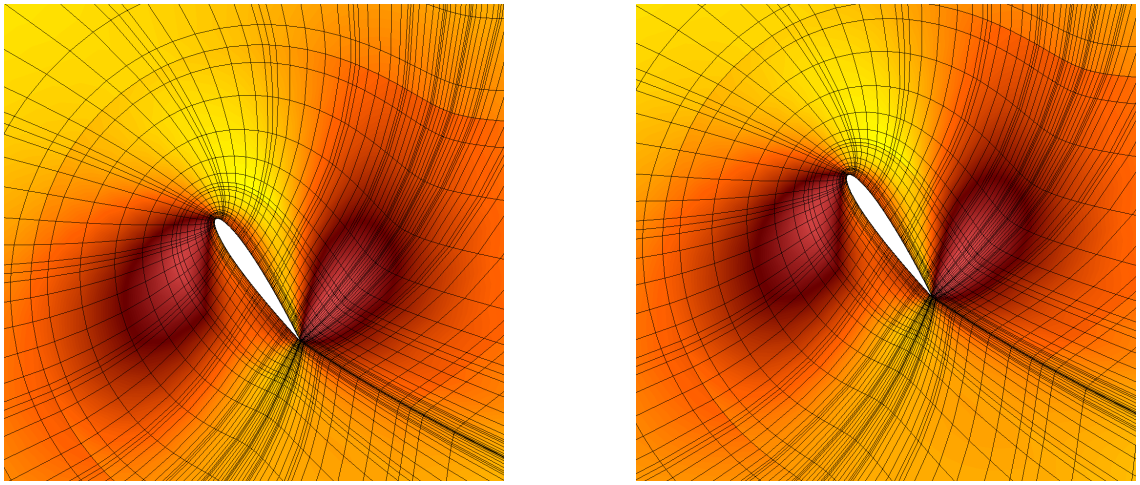
(d) t=7.5 (e) t=10.0 (f) t=12.5

(g) t=15.0 (h) t=17.5

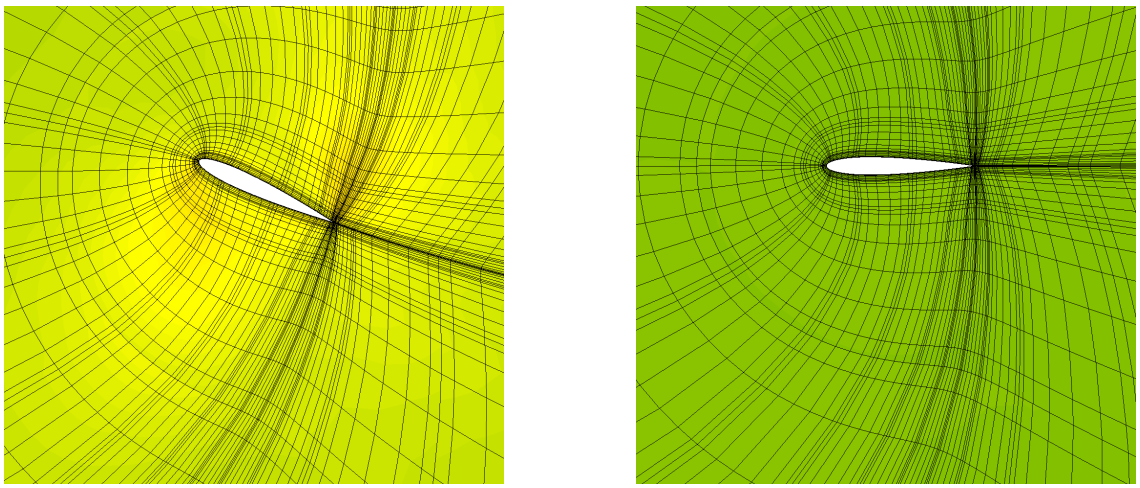
Figure 8: Images from terminal velocity fluid/6-DOF verification with center of gravity aft of the aerodynamic center



(a) $t = 0.0$ (b) $t = 0.4$

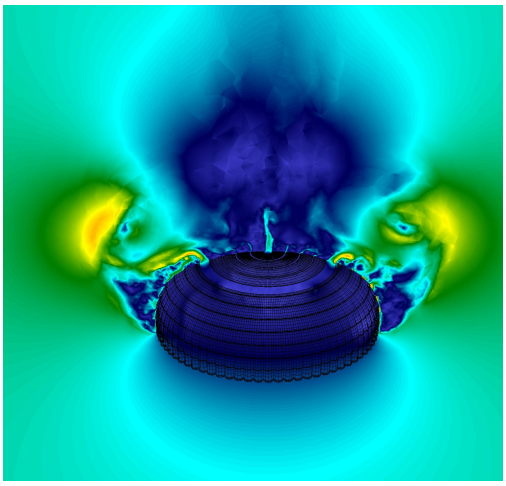


(c) $t = 0.8$ (d) $t = 1.2$

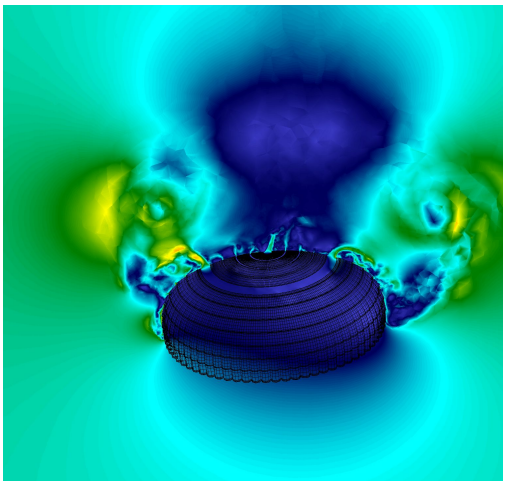


(e) $t = 1.6$ (f) $t = 2.0$

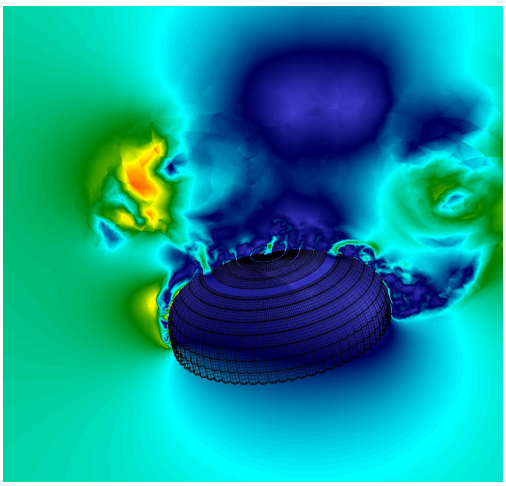
Figure 9: Heaving/Pitching Airfoil test case: Initial and displaced mesh at various temporal locations coloured with determinant of the deformation gradient tensor



(a) $t = 0.0$



(b) $t = 0.50$



(c) $t = 1.00$

Figure 10: Images from dynamic parachute simulation

moving body simulations by using a mesh with space-time elements which are curved to match the moving geometry. We have developed a six degree-of-freedom solver for performing rigid body simulations and a linear-elasticity approach for more general structural deformations. Preliminary verification results have been presented for moving-body simulations coupled with the 6-DOF solver or linear elasticity solver. Finally, we presented preliminary results from a dynamic parachute simulation.

The ultimate goal of this work is to perform simulations which can capture all of the relevant dynamics of the parachute motion. This works represents a small step in this direction. Future work will include verification of the coupling of the current solver with our shell structural solver, and focusing on performance through improving the linear and nonlinear solvers for tightly coupled FSI problems.

References

[1] Laslo T. Diosady and Scott M. Murman. Design of a variational multiscale method for turbulent compressible flows. AIAA Paper 2013-2870, 2013.

[2] Laslo T. Diosady and Scott M. Murman. Dns of flows over periodic hills using a discontinuous galerkin spectral element method. AIAA Paper 2014-2784, 2014.

[3] Laslo T. Diosady and Scott M. Murman. Tensor-product preconditioners for higher-order space-time discontinuous galerkin methods. 2014. under review.

[4] Laslo T. Diosady and Scott M. Murman. Higher-order methods for compressible turbulent flows using entropy variables. AIAA Paper 2015-0294, 2015.

[5] M. Ceze, L.T. Diosady, and S.M. Murman. Development of a high-order space-time matrix-free adjoint solver. AIAA 2016-0833, 2016.

[6] Laslo T. Diosady and Scott M. Murman. A linear-elasticity solver for higher-order space-time mesh deformation. AIAA Paper 2018-0919, 2018.

[7] Nicholas K. Burgess, Laslo T. Diosady, and Scott M. Murman. A c1-discontinuous-galerkin spectral-element shell structural solver. AIAA Paper 2017-3727, 2017.

[8] Corentin Carton De Wiart, Laslo T. Diosady, Anirban Garai, Nicholas Burgess, Patrick Blonigan, Dirk Ekelschot, and Scott M. Murman. Design of a modular monolithic implicit solver for multi-physics applications. AIAA Paper 2018-1400, 2018.

[9] Bjorn Hubner, Elmar Walhorn, and Dieter Dinkler. A monolithic approach to fluid-structure interaction using space-time finite elements. *Comput. Methods Appl. Mech. Engrg.*, 2004:2087–2104, 2004.

[10] C.M. Klaij, J.J.W. van der Vegt, and H. van der Ven. Space–time discontinuous galerkin method for the compressible navier–stokes equations. *Journal of Computational Physics*, 217:589–611, 2006.

[11] Matthias Heil, Andrew L. Hazel, and Jonathan Boyle. Solvers for large-displacement fluid–structure interaction problems: segregated versus monolithic approaches. *Computational Mechanics*, 43:91–101, 2008.

[12] E.H. van Brummelen, S.J. Hulshoff, and R. de Borst. A monolithic approach to fluid-structure interaction using space-time finite elements. *Comput. Methods Appl. Mech. Engrg.*, 2003:2727–2748, 2003.

[13] T. Tezduyar K. Stein and R. Benney. Mesh moving techniques for fluid-structure interactions with large displacements. *J. Appl. Mech*, 70(1):58–63, 2003.

[14] Tayfun E. Tezduyar and Sunil Sathe. Modelling of fluid-structure interactions with the space-time finite elements: Solution techniques. *Int. J. Numer. Meth. Fluids*, 54:855–900, 2007.

[15] L. Wang and P.-O. Persson. A high-order discontinuous galerkin method with unstructured space-time meshes for two-dimensional compressible flows on domains with large deformations. *Computers and Fluids*, 118:53–68, 2015.

[16] Michel Lesoinne and Charbel Farhat. Geometric conservation laws for flow problems with moving boundaries and deformable meshes, and their impact on aeroelastic computations. *Comput. Methods Appl. Mech. Engrg.*, 134:71–90, 1996.

[17] Robert E. Kirby, Zohar Yosibach, and George Em Karniadakis. Towards stable coupling methods for high-order discretizations of fluid-structure interaction: Algorithms and observations. *Journal of Computational Physics*, 223:489–518, 2007.

[18] David Keyes, Lois Curfman McInnes, and CarolWoodward. Multiphysics simulations: Challenges and opportunities. Argonne National Laboratory ANL/MCS-TM-321, 2011.

[19] Farzad Ismail and Philip L. Roe. Affordable, entropy-consistent euler flux functions ii: entropy production at shocks. *J. Comput. Phys.*, 228(15):5410–5436, August 2009.

[20] F. Bassi and S. Rebay. GMRES discontinuous Galerkin solution of the compressible Navier-Stokes equations. In Karniadakis Cockburn and Shu, editors, *Discontinuous Galerkin Methods: Theory, Computation and Applications*, pages 197–208. Springer, Berlin, 2000.

[21] Timothy J. Barth. Numerical methods for gasdynamic systems on unstructured meshes. In D. Kroner, M. Olhberger, and C. Rohde, editors, *An Introduction to Recent Developments in Theory and Numerics for Conservation Laws*, pages 195 – 282. Springer-Verlag, 1999.

[22] Scott M. Murman, Michael J. Aftomis, and Marsha J. Berger. Simulations of 6-dof motion with a cartesian method. AIAA 2003-1246, 2003.

[23] Z.J. Wang, K. Fidkowski, R. Abgrall, F. Bassi, D. Caraeni, A. Cary, H. Deconinck, R. Hartmann, K. Hillewaert, H.T. Huynh, N. Kroll, G. May, P.-O. Persson, B. van Leer, and M. Visbal. High-order cfd methods: Current status and perspective. *International Journal for Numerical Methods in Fluids*, 72:811–845, 2013.

[24] P.-O. Persson and K. Fidkowski. Results from the 5th International Workshop on Higher-Order CFD Methods: Test case CL1. 2018.

[25] Ricardo Machin and Eric Ray. Pendulum motion in main parachute clusters. AIAA Paper 2015-2138, 2015.